Inorganic Chemistry

Article

Crystal Field Effects on the Optical Absorption and Luminescence Properties of Ni^{2+}-Doped Chlorides and Bromides: Crossover in the Emitting Higher Excited State

Oliver S. Wenger, Sophie Bénard, and Hans U. Güdel*

Departement für Chemie und Biochemie, Universität Bern, Freiestrasse 3, CH-3000 Bern 9, Switzerland

Single crystals of $CsCdCl_3$, $CsCdBr_3$, $CsMgBr_3$, and $MgBr_2$ doped with 0.1/5% Ni^{2+} were grown by the Bridgman technique and studied by variable-temperature optical absorption and luminescence spectroscopies. At cryogenic temperatures all these systems are dual emitters; i.e., they emit light from two distinct, thermally nonequilibrated excited states. The emitting higher excited state is $^1T_{2g}$ in Ni^{2+}:$CsCdCl_3$ and Ni^{2+}:$CsCdBr_3$ and $^1A_{1g}$ in Ni^{2+}:$CsMgBr_3$ and Ni^{2+}:$MgBr_2$. This crossover manifests itself in a change from red broad-band to yellow sharp-line luminescence, and it is rationalized on the basis of crystal field theory. Temperature-dependent luminescence as well as two-color pump and probe experiments reveal that in Ni^{2+}:$CsMgBr_3$ and Ni^{2+}:$MgBr_2$ the $^1T_{2g}$ state lies only about 70 and 170 cm^{-1}, respectively, above $^1A_{1g}$. The effect of crystal field strength on thermally activated nonradiative multiphonon relaxation processes in the bromides is examined for both $^1A_{1g}$/$^1T_{2g}$ higher excited state and $^3T_{2g}$ first excited-state emission. Two-color excited-state excitation experiments are used to monitor Ni^{2+} excited-state absorption transitions originating from $^3T_{2g}$.

I. Introduction

The optical spectroscopic properties of Ni^{2+} complexes and Ni^{2+}-doped materials have received a great deal of attention in the literature.[1] The interest in materials in which Ni^{2+} dopants are in (approximate) octahedral coordination has been 2-fold. On one hand, their near-infrared (NIR) laser potential has been intensively explored.[2] In 1963, pulsed NIR laser operation of cryogenically cooled Ni^{2+}:MgF_2 was reported,[3] and this was the first example of a laser with broad-band tuning capability. On the other hand, at cryogenic temperatures these materials exhibit luminescence from more than one excited state. This has been shown to be the case in oxides,[4] fluorides,[5] and chlorides[6] as well as bromides.[7] Light emission from multiple excited states is a rare phenomenon among transition metal systems. To date, among octahedrally coordinated transition metal ions only Ti^{2+}, Mo^{3+}, Re^{4+}, and Os^{4+} are known to exhibit multiple emissions when doped into appropriate host lattices.[8] Thus, Ni^{2+}-doped materials have been in the focus of several NIR to visible (VIS) photon upconversion studies.[9] Regarding luminescence properties, Ni^{2+}-doped bromides have so far received little attention. Only Ni^{2+}:$CsCdBr_3$ and the mixed-

(1) (a) Lever, A. B. P. *Inorganic Electronic Spectroscopy*, 2nd ed.; Elsevier: Amsterdam, 1984. (b) Henderson, B.; Imbusch, G. F. *Optical Spectroscopy of Inorganic Solids*; Oxford Science Publications: Oxford, U.K., 1989.
(2) (a) Kück, S. *Appl. Phys. B* **2001**, *72*, 515−562. (b) Koetke, J.; Petermann, K.; Huber, G. *J. Lumin.* **1993**, *60−61*, 197−200. (c) Moncorgé, R.; Benyattou, T. *Phys. Rev. B* **1988**, *37*, 9186−9196.
(3) Johnson, L. F.; Dietz, R. E.; Guggenheim, H. J. *Phys. Rev. Lett.* **1963**, *11*, 318−320.

(4) (a) Ralph, J. E.; Townsend, M. G. *J. Phys. C* **1970**, *3*, 8−18. (b) Vehse, W. E.; Lee, K. H.; Yun, S. J.; Sibley, W. A. *J. Lumin.* **1975**, *10*, 149−162.
(5) (a) Iverson, M. V.; Sibley, W. A. *J. Lumin.* **1979**, *20*, 311−324. (b) Ferguson, J.; Masui, H. *J. Phys. Soc. Jpn.* **1977**, *42*, 1640−1646. (c) May, P. S.; Güdel, H. U. *Chem. Phys. Lett.* **1990**, *175*, 488−492.
(6) May, P. S.; Güdel, H. U. *J. Chem. Phys.* **1991**, *95*, 6343−6354.
(7) de Viry, D.; Tercier, N.; Denis, J. P.; Blanzat, B.; Pellé, F. *J. Chem. Phys.* **1992**, *97*, 2263−2270.
(8) (a) Gamelin, D. R.; Güdel, H. U. *Acc. Chem. Res.* **2000**, *33*, 235−242. (b) Jacobsen, S. M.; Güdel, H. U. *J. Lumin.* **1989**, *43*, 125−137. (c) Gamelin, D. R.; Güdel, H. U. *J. Phys. Chem. B* **2001**, *44*, 10222−10234. (d) Gamelin, D. R.; Güdel, H. U. *J. Am. Chem. Soc.* **1998**, *120*, 12143−12144. (e) Gamelin, D. R.; Güdel, H. U. *Inorg. Chem.* **1999**, *38*, 5154−5164. (f) Wermuth, M.; Güdel, H. U. *J. Am. Chem. Soc.* **1999**, *121*, 10102−10111.
(9) (a) Oetliker, U.; Riley, M. J.; May, P. S.; Güdel, H. U. *Coord. Chem. Rev.* **1991**, *91*, 125−130. (b) May, P. S.; Güdel, H. U. *J. Lumin.* **1990**, *47*, 19−25. (c) Wenger, O. S.; Gamelin, D. R.; Güdel, H. U. *J. Am. Chem. Soc.* **2000**, *122*, 7408−7409.
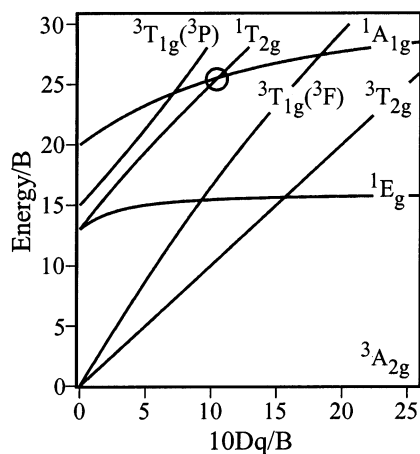
Figure 1. Energy level diagram for octahedrally coordinated d⁸ ions[11] calculated using $C/B = 4.0$.

halide system Ni²⁺:CsCdBrCl₂ have been demonstrated to exhibit luminescence from a higher excited state.[7,10] Ni²⁺ has the 3d⁸ electron configuration. Figure 1 exhibits an energy level diagram for octahedrally coordinated d⁸ ions.[11] In Ni²⁺-doped fluorides and chlorides the crystal field is such that $10Dq/B$ crystal field parameter ratios range from 7.3 to 8.8.[12] At cryogenic temperatures these materials exhibit higher excited-state luminescence originating from the $^1T_{2g}$ state. In this paper we demonstrate that in Ni²⁺-doped bromides substantially higher $10Dq/B$ ratios may be achieved, leading to a crossover in the emitting higher excited state from $^1T_{2g}$ to $^1A_{1g}$; see the circle in Figure 1. Among octahedrally coordinated transition metal systems such chemically induced crossovers in an emitting d−d excited state have previously been reported for Ti²⁺-,[13] V³⁺-,[14] and Cr³⁺-doped systems[15] but never before in an emitting higher excited state. The fact that luminescence transitions to a total number of 4 energetically lower lying electronic states originate from the Ni²⁺ $^1T_{2g}/^1A_{1g}$ states allows us to obtain an unusually complete picture of the effects of this crossover on both radiative and nonradiative relaxation processes. The fact that the $^3T_{2g}$ first excited state is metastable, too, allows us to study the $^1T_{2g}/^1A_{1g}$ crossover by means of two-color pump and probe luminescence excitation experiments. Thus, the crystal field effects in our systems can be studied by both one- and two-photon spectroscopic techniques, and they yield complementary information.

In this study we examine the systems Ni²⁺:MgBr₂, Ni²⁺:CsMgBr₃, Ni²⁺:CsCdBr₃, and Ni²⁺:CsCdCl₃. The local environments of the divalent cations in all these systems are similar in that they all consist of trigonally distorted $M^{II}X_6^{4-}$

octahedra. The Ni²⁺ dopant ions substitute for Mg²⁺ and Cd²⁺, respectively. MgBr₂ crystallizes in the hexagonal space group $P\bar{3}m1$ and adopts the so-called Cd(OH)₂ layer structure type. The site symmetry of Mg²⁺ is D_{3d}.[16] CsMgBr₃ and CsCdBr₃ crystallize in the hexagonal space group $P6_3/mmc$ and belong to the linear-chain CsNiCl₃ structure type.[17,18] The site symmetry of Mg²⁺/Cd²⁺ is D_{3d}. CsCdCl₃ crystallizes in the $P6_3/mmc$ space group, too, but it has two types of CdCl₆⁴⁻ octahedra, and its structure is an intermediate between the CsNiCl₃ and the KNiF₃ structure types.[19] The Cd²⁺ site symmetries in this host are D_{3d} and C_{3v}, respectively, but at low dopant concentrations Ni²⁺ only substitutes into the smaller C_{3v} site.[20]

II. Experimental Section

The methods of sample preparation and crystal growth used for these investigations have been described elsewhere.[21] All crystals used are somewhat hygroscopic, and therefore, they were kept under inert atmosphere for all measurements as described in ref 22. The nominal Ni²⁺ dopant concentrations in the crystals used for the spectroscopic measurements were 5% for absorption and 0.1% for luminescence experiments. All crystals used in this study were cut perpendicular to the crystallographic c-axis. Thus, all spectra presented in this work are so-called axial spectra.

Absorption spectra were measured on a Cary 5e (Varian) spectrometer. Continuous-wave (cw) survey luminescence measurements were performed using the 488 nm line of an Ar⁺ laser (Ion Laser Technology). The sample luminescence was dispersed by a 3/4 m single monochromator (Spex 1702) equipped with 600 grooves/mm gratings blazed at 750, 1250, and 1600 nm. Ni²⁺ luminescence between 550 and 1000 nm was detected with a cooled red-sensitive photomultiplier tube (Hamamatsu P3310-01) connected to a photon counting system (Stanford Research 400). Luminescences at longer wavelengths were detected using a liquid-nitrogen-cooled Ge detector (ADC 403L) or a dry-ice-cooled PbS detector (Hamamatsu P3337) connected to a lock-in amplifier.

Two-color excited-state excitation (ESE) experiments were performed using two Ar⁺ laser pumped tunable Ti³⁺:sapphire lasers (Spectra Physics 3900S). Wavelength control was achieved with a step-motor driven birefringent filter and a wavemeter (Burleigh WA2100). The wavelength dependence of the laser power was measured on a powermeter (Coherent Labmaster) simultaneously with the excitation scans. Typical laser powers used were ≈200 mW for the pump laser and ≈1 mW for the probe laser, respectively. The Ni²⁺ $^1A_{1g}/^1T_{2g} \rightarrow {}^3A_{2g}$ higher excited-state luminescence was dispersed by a 0.85 m double monochromator equipped with 500 nm blazed (1200 grooves/mm) gratings and detected with a PMT as described above.

For Ni²⁺ $^1A_{1g}/^1T_{2g}$ lifetime measurements the Ar⁺ laser beam was passed through an accousto-optic modulator (Coherent 305) connected to a function generator (Stanford Research DS345). The

(10) Lüthi, S. R.; Riley, M. J. *Inorg. Chem.* **2001**, *40*, 196−207.
(11) Sugano, S.; Tanabe, Y.; Kamimura, H. *Multiplets of Transition Metal Ions in Crystals*; Academic Press: New York/London, 1970.
(12) (a) Ferguson, J.; Guggenheim, H. J.; Wood, P. L. *J. Chem. Phys.* **1964**, *40*, 822−830. (b) Martins, E.; Vieira, N. D., Jr.; Baldochi, S. L.; Morato, S. P.; Gesland, J. Y. *J. Lumin.* **1994**, *62*, 281−289. (c) McPherson, G. L.; Stucky, G. D. *J. Chem. Phys.* **1972**, *57*, 3780−3786.
(13) Wenger, O. S.; Güdel, H. U. *Inorg. Chem.* **2001**, *40*, 5747−5753.
(14) Reber, C.; Güdel, H. U. *J. Lumin.* **1988**, *42*, 1−13.
(15) (a) de Viry, D.; Denis, J. P.; Tercier, N.; Blanzat, B. *Solid State Commun.* **1987**, *63*, 1183−1187. (b) Dolan, J. F.; Kappers, L. A.; Bartram, R. H. *Phys. Rev. B* **1986**, *33*, 7339−7341.
(16) Wyckoff, R. W. G. *Crystal Structures*, 2nd ed.; Interscience Publishers: New York, 1965; Vol. 1.
(17) McPherson, G. L.; McPherson, A. M.; Atwood, J. L. *J. Phys. Chem. Solids* **1980**, *41*, 495−499.
(18) McPherson, G. L.; Koch, R. C.; Stucky, G. D. *J. Chem. Phys.* **1974**, *60*, 1424−1431.
(19) Chang, J. R.; McPherson, G. L.; Atwood, J. L. *Inorg. Chem.* **1975**, *14*, 3079−3085.
(20) Oetliker, U.; Riley, M. J.; Güdel, H. U. *J. Lumin.* **1995**, *63*, 63−73.
(21) May, P. S.; Güdel, H. U. *J. Lumin.* **1990**, *46*, 277−290.
(22) Wenger, O. S.; Valiente, R.; Güdel, H. U. *Phys. Rev. B* **2001**, *64*, 235116/1−8.

Table 1. Experimental Energies E and Oscillator Strengths f of Ni^{2+} Absorption Transitions in Figure 2

state	$Ni^{2+}:CsCdCl_3$		$Ni^{2+}:CsCdBr_3$		$Ni^{2+}:CsMgBr_3$		$Ni^{2+}:MgBr_2$	
	E/cm^{-1}	$10^{-5}f$	E/cm^{-1}	$10^{-5}f$	E/cm^{-1}	$10^{-5}f$	E/cm^{-1}	$10^{-5}f$
$^3A_{2g}$	0		0		0		0	
$^3T_{2g}$	6 210	0.9	6 540	2.1	6 610	1.7	6 720	1.4
$^3T_{1g}(^3F)$	10 600	1.3	11 210	3.4	11 240	3.9	11 420	3.2
^1E_g	12 570	0.1	11 780		11 800		11 940	
$^1A_{1g}$	19 029	0.01	16 930	0.06	17 080	0.04	17 335	0.04
$^1T_{2g}$	18 204	0.2	17 710	1.0	17 940	1.5	18 270	1.3
$^3T_{1g}(^3P)$	20 516	4.5	20 320	10.8	20 515	10.8	20 710	10.1

luminescence decay curves were recorded on a multichannel scaler (Stanford Research 430).

Sample cooling was achieved by a closed-cycle He cryostat (Air Products Displex) for absorption measurements and with a He gas flow technique for the luminescence experiments.

All luminescence spectra were corrected for the wavelength-dependent sensitivity of the monochromator and the detection system and were converted to photon counts versus wavenumber using the procedure described in ref 23.

III. Results

Figure 2 shows 15 K axial survey absorption spectra of (a) 5% $Ni^{2+}:CsCdCl_3$, (b) 5% $Ni^{2+}:CsCdBr_3$, (c) 5% $Ni^{2+}:CsMgBr_3$, and (d) 5% $Ni^{2+}:MgBr_2$. Each spectrum exhibits 6 d–d absorption bands, and within the octahedral approximation their assignment is straightforward with the Tanabe–Sugano diagram in Figure 1.[11] The band maximum energies as well as absorption oscillator strengths are collected in Table 1. In the bromides the oscillator strengths are about a factor of 2 higher than in the chloride. For our study the most important difference between the chloride and the bromide spectra lies in the 17000–19000 cm^{-1} spectral region. In $Ni^{2+}:CsCdCl_3$ (a) the $^1T_{2g}$ absorption band maximum is 825 cm^{-1} *below* the $^1A_{1g}$ maximum. In $Ni^{2+}:CsCdBr_3$, $Ni^{2+}:CsMgBr_3$, and $Ni^{2+}:MgBr_2$ the $^1T_{2g}$ band maximum is 780, 860, and 935 cm^{-1} *above* the $^1A_{1g}$ maximum.

Figure 3 shows 15 K axial survey luminescence spectra of (a) 0.1% $Ni^{2+}:CsCdCl_3$, (b) 0.1% $Ni^{2+}:CsCdBr_3$, (c) 0.1% $Ni^{2+}:CsMgBr_3$, and (d) 0.1% $Ni^{2+}:MgBr_2$. Excitation occurred into $^3T_{1g}(^3P)$ at 20 492 cm^{-1} (Figure 2). The dominant luminescence band in all four spectra peaks is around 4000–5000 cm^{-1}, and it is assigned to $^3T_{2g} \rightarrow {}^3A_{2g}$ emission. All luminescence bands above 5500 cm^{-1} are due to Ni^{2+} higher excited state emission (vide infra). Particularly in the vis spectral range $Ni^{2+}:CsCdCl_3$ (a) and $Ni^{2+}:CsCdBr_3$ (b) exhibit distinctly different 15 K luminescences from $Ni^{2+}:CsMgBr_3$ (c) and $Ni^{2+}:MgBr_2$ (d). The former show broad-band vis luminescence, whereas the latter mainly emit in a sharp line centered around 17 000 cm^{-1}. In $Ni^{2+}:CsMgBr_3$ (c), however, some weak broad-band vis 15 K luminescence centered around 15 600 cm^{-1} is also observed but not in $Ni^{2+}:MgBr_2$ (d).

The upper trace in Figure 4 shows a 15 K high-resolution absorption spectrum (axial) of 5% $Ni^{2+}:MgBr_2$ in the spectral region of the $^3A_{2g} \rightarrow {}^1A_{1g}$ transition. The lower trace in Figure 4 shows an axial 15 K high-resolution vis luminescence
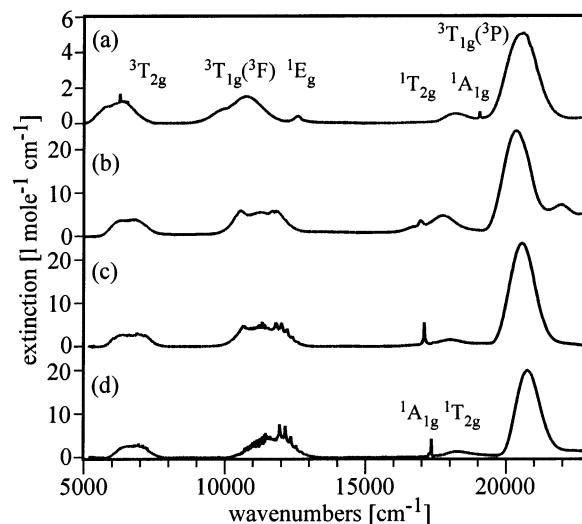
(23) Ejder, J. *J. Opt. Soc. Am.* **1969**, *59*, 223–224.

Figure 2. The 15 K axial survey d–d absorption spectra of 5% Ni^{2+}-doped CsCdCl$_3$ (a), CsCdBr$_3$ (b), CsMgBr$_3$ (c), and MgBr$_2$ (d). Note the different scales in (a) and (b)–(d).
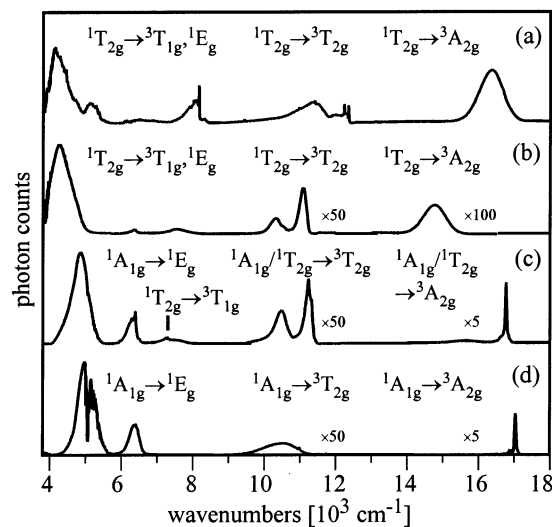

Figure 3. The 15 K axial survey luminescence spectra of 0.1% Ni^{2+}-doped CsCdCl$_3$ (a), CsCdBr$_3$ (b), CsMgBr$_3$ (c), and MgBr$_2$ (d) obtained after excitation at 20 492 cm^{-1}. Note the scaling factors in (b)–(d).

spectrum of 0.1% $Ni^{2+}:MgBr_2$ obtained after excitation at 20 492 cm^{-1}. The two spectra exhibit a relatively close image–mirror image relation. Both spectra are essentially comprised of a series of 5 lines in a range of roughly 90 cm^{-1} (lines 1a–5a in absorption and 1e–5e in luminescence, respectively) and a sixth line (6a/6e) located roughly 150 cm^{-1} above (6a) and below (6e) the most intense line. The energies of these lines are listed in Table 2.
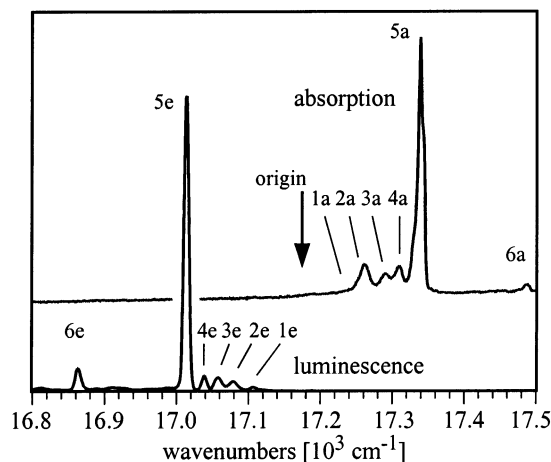
Figure 4. High-resolution $^3A_{2g} \leftrightarrow {}^1A_{1g}$ absorption and luminescence spectra of 5%/0.1% Ni²⁺:MgBr₂ at 15 K (axial). The arrow indicates the energetic position of the electronic $^1A_{1g}$ origin. The labels of the individual absorption and luminescence lines refer to Table 2.
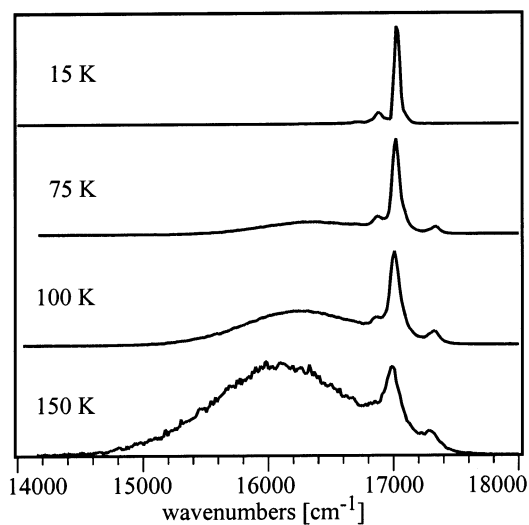

Figure 5. Vis luminescence spectra of 0.1% Ni²⁺:MgBr₂ obtained after excitation at 20 492 cm⁻¹ at various temperatures. All spectra are arbitrarily scaled.

Table 2. Energies E, Energy Differences ΔE to the Electronic Origin at 17 175 cm⁻¹, and Assignments of the $^3A_{2g} \leftrightarrow {}^1A_{1g}$ Absorption and Luminescence Lines of Ni²⁺:MgBr₂ at 15 K with All Data Extracted from Figure 4

absorption			luminescence			
label	E/cm⁻¹	ΔE/cm⁻¹	label	E/cm⁻¹	ΔE/cm⁻¹	assignment[a]
1a	17 237	+62	1e	17 106	−69	
2a	17 264	+89	2e	17 079	−96	
3a	17 288	+113	3e	17 058	−117	e_{1u}
4a	17 311	+136	4e	17 039	−136	
5a	17 338	+163	5e	17 012	−163	a_{2u}
6a	17 484	+309	6e	16 863	−312	$a_{2u} + a_{1g}$

[a] The assignment of vibronic origins is made on the basis of published IR data on CsNiBr₃.[36]

Figure 5 shows the temperature dependence of the vis luminescence of 0.1% Ni²⁺:MgBr₂. All spectra are arbitrarily scaled. Excitation occurred at 20 492 cm⁻¹. At 15 K there is only sharp-line (S) vis luminescence centered around 17 000 cm⁻¹. At temperatures above 50 K there is additional broad-band (B) luminescence centered around 16 100 cm⁻¹. With increasing temperature the broad-band luminescence
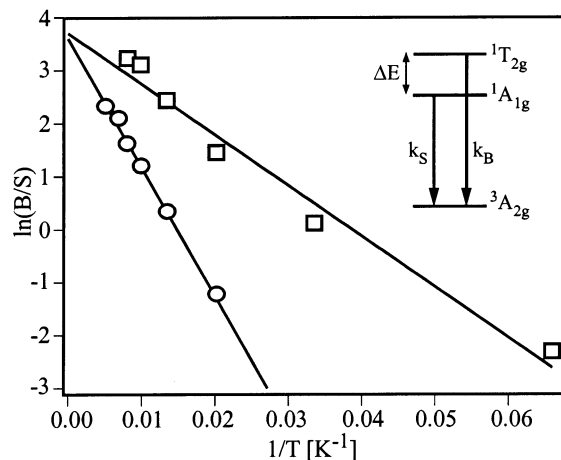

Figure 6. Broad-band (B) $^1T_{2g} \rightarrow {}^3A_{2g}$ versus sharp-line (S) $^1A_{1g} \rightarrow {}^3A_{2g}$ luminescence intensity ratios plotted on a logarithmic scale versus $1/T$ for 0.1% Ni²⁺:MgBr₂ (circle markers) and 0.1% Ni²⁺:CsMgBr₃ (square markers). The lines are linear regression fits with slopes of 243 and 96 K, respectively. The inset illustrates the simplified model used to analyze these data (see section IVC).
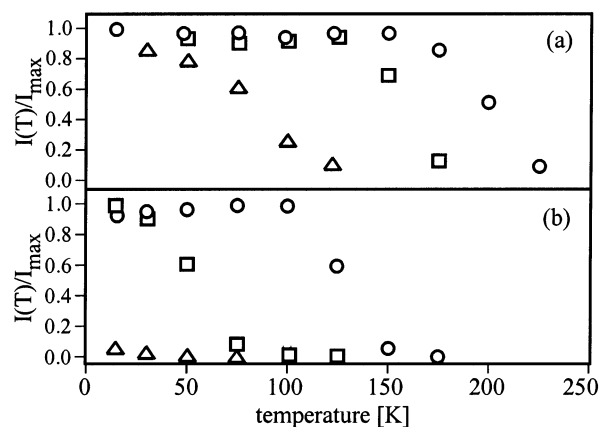

Figure 7. Temperature dependence of the normalized integrated $^3T_{2g} \rightarrow {}^3A_{2g}$ (a) and $^1A_{1g}/^1T_{2g} \rightarrow {}^3A_{2g}$ (b) luminescence intensities in 0.1% Ni²⁺-doped CsCdBr₃ (triangles), CsMgBr₃ (squares), and MgBr₂ (circles). Excitation occurred at 11 500 cm⁻¹ for $^3T_{2g}$ emission (a) and at 20 492 cm⁻¹ for $^1A_{1g}/^1T_{2g}$ emission (b).

intensity increases at the expense of sharp-line luminescence; i.e., the photon ratio B/S increases. The same is true for 0.1% Ni²⁺:CsMgBr₃ (temperature-dependent spectra not shown), but in this system the broad-band luminescence intensity is nonnegligible already at 15 K.

This is shown in Figure 6, which plots $\ln(B/S)$ for 0.1% Ni²⁺:CsMgBr₃ (square markers) and 0.1% Ni²⁺:MgBr₂ (circle markers) as a function of inverse temperature ($1/T$). The increase of the ratio B/S with temperature is more pronounced for 0.1% Ni²⁺:MgBr₂ than for 0.1% Ni²⁺:CsMgBr₃.

Figure 7 exhibits the temperature dependence of the normalized integrated NIR $^3T_{2g} \rightarrow {}^3A_{2g}$ (a) and vis $^1T_{2g}/^1A_{1g} \rightarrow {}^3A_{2g}$ luminescence intensity (b) in 0.1% Ni²⁺:CsCdBr₃ (triangles), 0.1% Ni²⁺:CsMgBr₃ (squares), and 0.1% Ni²⁺:MgBr₂ (circles). All luminescence intensities were normalized to a maximum value of 1, except for the 0.1% Ni²⁺:CsCdBr₃ data points in Figure 7b (triangles), for reasons discussed in section IVD. Excitation occurred at 11 500 cm⁻¹ into $^3T_{1g}(^3F)$ (Figure 7a) and at 20492 cm¹ into $^3T_{1g}(^3P)$ (Figure 7b), respectively. All data are corrected for the temperature
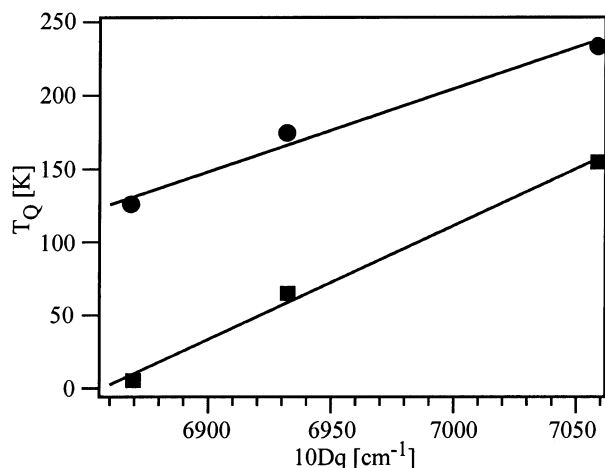
Figure 8. Plot of the quenching temperatures $T_Q(^3T_{2g})$ (filled circles) for NIR $^3T_{2g} \rightarrow \, ^3A_{2g}$ emission and $T_Q(^1T_{2g}/^1A_{1g})$ (filled squares) for vis $^1A_{1g}/^1T_{2g} \rightarrow \, ^3A_{2g}$ emission in 0.1% Ni^{2+}:CsCdBr$_3$, 0.1% Ni^{2+}:CsMgBr$_3$, and 0.1% Ni^{2+}:MgBr$_2$ as a function of the crystal field strength $10Dq$ in these systems. T_Q is defined in section III. The $10Dq$ values are calculated in section IVA, and they are listed in Table 3. The lines are linear regression fits to the two T_Q data sets.

Table 3. Octahedral Crystal Field Parameters Obtained for Ni^{2+} in Various Hosts from Crystal Field Calculations Using the Absorption Band Maximum Energies Listed in Table 1[27]

	Ni^{2+}:CsCdCl$_3$	Ni^{2+}:CsCdBr$_3$	Ni^{2+}:CsMgBr$_3$	Ni^{2+}:MgBr$_2$
$10Dq$/cm^{-1}	6340	6869	6932	7059
B/cm^{-1}	799	716	720	720
C/B	3.93	3.93	3.93	4.04

dependencies of the absorption cross sections at these two energies. All luminescence intensities are reduced drastically upon increasing temperature. This thermally induced luminescence quenching can be quantified by defining the quenching temperature T_Q as the temperature at which the luminescence intensity is reduced to 10% of its maximum value.[24] For $^3T_{2g} \rightarrow \, ^3A_{2g}$ luminescence $T_Q(^3T_{2g})$ increases from 125 to 175 to 225 K along the series Ni^{2+}:CsCdBr$_3$, Ni^{2+}:CsMgBr$_3$, and Ni^{2+}:MgBr$_2$. For $^1T_{2g}/^1A_{1g} \rightarrow \, ^3A_{2g}$ luminescence $T_Q(^1T_{2g}/^1A_{1g})$ increases from 5 to 65 to 145 K along the same series.

Figure 8 plots these $T_Q(^3T_{2g})$ (filled circles) and $T_Q(^1T_{2g}/^1A_{1g})$ (filled squares) values as a function of $10Dq$ in the three bromide systems Ni^{2+}:CsCdBr$_3$, Ni^{2+}:CsMgBr$_3$, and Ni^{2+}:MgBr$_2$. The $10Dq$ values are calculated in section IVA, and they are listed in Table 3. Both $T_Q(^3T_{2g})$ and $T_Q(^1T_{2g}/^1A_{1g})$ increase linearly with increasing $10Dq$.

Figure 9 shows 15 K excited-state excitation (ESE) spectra of (a) 0.1% Ni^{2+}:CsCdBr$_3$, (b) 0.1% Ni^{2+}:CsMgBr$_3$, and (c) 0.1% Ni^{2+}:MgBr$_2$. These spectra were obtained from pump/probe experiments as follows. A strong pump laser source at 11 000 cm^{-1} provides a nonzero $^3T_{2g}$ population. A weak probe laser is scanned between 11 000 and 14 400 cm^{-1} while the $^1T_{2g}/^1A_{1g} \rightarrow \, ^3A_{2g}$ higher excited-state luminescence intensity around 15 000/17 000 cm^{-1} is monitored (Figure 3). Thus, $^3T_{2g}$ excited-state absorption (ESA) transitions can be detected. Several ESA bands are observed in each spectrum of Figure 9. All ESA band maximum energies
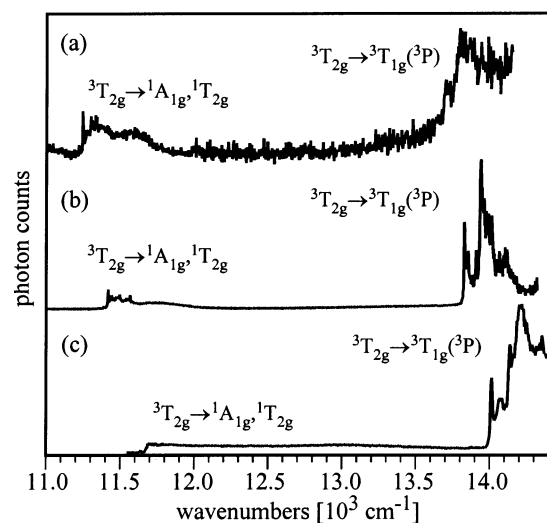
(24) Reber, C.; Güdel, H. U. *J. Lumin.* **1990**, *47*, 7−18.

Figure 9. The 15 K axial Ni^{2+} $^3T_{2g} \rightarrow \, ^1A_{1g}$, $^1T_{2g}$, and $^3T_{1g}(^3P)$ excited-state excitation (ESE) spectra of 0.1% Ni^{2+}:CsCdBr$_3$ (a), 0.1% Ni^{2+}:CsMgBr$_3$ (b), and 0.1% Ni^{2+}:MgBr$_2$ (c). See sections II/III for experimental details.
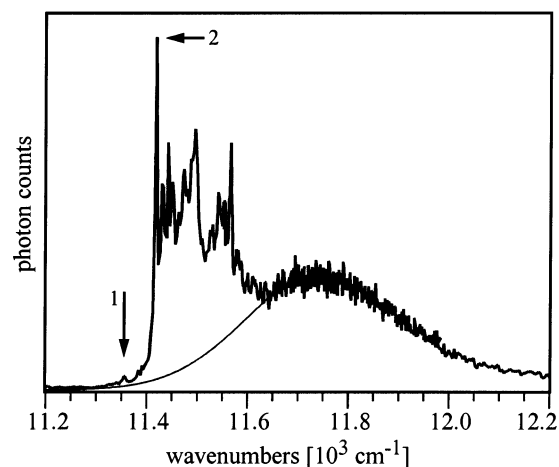

Figure 10. High-resolution $^3T_{2g} \rightarrow \, ^1A_{1g}$, $^1T_{2g}$ excited-state excitation (ESE) spectrum of 0.1% Ni^{2+}:CsMgBr$_3$ at 15 K (axial). The arrows indicate the electronic $^3T_{2g} \leftrightarrow \, ^1A_{1g}$ (no. 1) and $^3T_{2g} \leftrightarrow \, ^1T_{2g}$ origins (no. 2). The faint smooth line shows the extrapolated band shape of the $^3T_{2g} \rightarrow \, ^1A_{1g}$ transition in the 11 300−11 640 cm^{-1} spectral range.

increase along the series Ni^{2+}:CsCdBr$_3$, Ni^{2+}:CsMgBr$_3$, and Ni^{2+}:MgBr$_2$.

Figure 10 shows the lower energetic 15 K ESA bands of 0.1% Ni^{2+}:CsMgBr$_3$ from Figure 9b in more detail. This spectrum is comprised of two vastly different parts. A series of about 15 sharp lines is centered at about 11 480 cm^{-1} spanning an energy range of about 250 cm^{-1}, and a substantially broader unstructured band is centered around 11 740 cm^{-1}. The lowest energetic line occurs at 11 355 cm^{-1} (arrow 1), and the first intense line peaks at 11 418 cm^{-1} (arrow 2).

IV. Analysis and Discussion

A. Energy Level Structure: Crystal Field Analysis. Although in all of the systems considered here the spectroscopically active NiX$_6^{4-}$ units are trigonally distorted (vide supra), the main crystal field effects when changing from one lattice to another can be adequately described within the purely octahedral approximation. The energies of the

$^3A_{2g} \rightarrow {}^3T_{2g}$ absorption band maxima in Figure 2 are a direct measure for the octahedral crystal field parameters $10Dq$.[25] Figure 2 shows that the $^3T_{2g}$ absorption maximum is blue-shifted along the series Ni^{2+}:CsCdCl$_3$, Ni^{2+}:CsCdBr$_3$, Ni^{2+}:CsMgBr$_3$, and Ni^{2+}:MgBr$_2$; i.e., $10Dq$ increases. The $^3A_{2g} \rightarrow {}^1E_g$ and the $^3A_{2g} \rightarrow {}^1A_{1g}$ transitions, on the other hand, have only a weak $10Dq$ dependence, but they are strongly dependent on the Racah parameters.[10] The ^1E_g and $^1A_{1g}$ absorption bands are at substantially lower energies in the bromides than in Ni^{2+}:CsCdCl$_3$. In the bromides the ^1E_g absorption merges with the $^3T_{1g}(^3F)$ band, and particularly in the case of Ni^{2+}:CsMgBr$_3$, Figure 2c, and Ni^{2+}:MgBr$_2$, Figure 2d, this gives rise to $^3T_{1g}(^3F)-{}^1E_g$ spinor interaction effects, resulting in absorption bands with pronounced vibrational fine structure. This effect is well documented in the literature of Ni^{2+} systems.[26] More important for our study is the fact that the $^1A_{1g}$ state is red-shifted in the bromides relative to the chloride by roughly 2000 cm^{-1}, Table 1, indicating a substantial reduction of the Racah parameters.

The crystal field effects on the energy level structure can be quantified by a simple O_h crystal field calculation.[27] Using the 15 K absorption band maximum energies listed in Table 1, for each system a set of 3 crystal field parameters ($10Dq$, B, C) is calculated by means of a least-squares fit procedure. The resulting parameters are listed in Table 3. In the order from Ni^{2+}:CsCdCl$_3$ to Ni^{2+}:CsCdBr$_3$ $10Dq$ increases by 5%. This effect has been analyzed within the framework of the differential nephelauxetic effect in ref 10. Briefly, the t$_{2g}$- and e$_g$-orbital energies are affected differently by increasing metal–ligand bond covalency. This is the case when replacing Cl$^-$ ligands by Br$^-$, and it leads to an increase in the t$_{2g}$–e$_g$ energy splitting. The increase in $10Dq$ when going from Ni^{2+}:CsCdBr$_3$ to Ni^{2+}:CsMgBr$_3$ and Ni^{2+}:MgBr$_2$ is attributed to the smaller dopant sites in the Mg^{2+} host crystals compared to CsCdBr$_3$.[28] The Racah B parameter is roughly 800 cm^{-1} in the chloride and 720 cm^{-1} in the bromides, with C/B close to 4 in all cases; see Table 3. This 10% reduction in the Racah parameters reflects the more covalent nature of the Ni^{2+}–X$^-$ bond in the bromides; i.e., it is a direct manifestation of the nephelauxetic effect.[29] In the free Ni^{2+} ion $B = 1030$ cm^{-1};[30] i.e., the nephelauxetic parameter β is 0.7 for the bromides. We point out that in our simple crystal field calculation experimental and calculated $^1A_{1g}$ energies agree only within roughly 10%, whereas for all other excited-state energies in Table 1 this agreement is one order of magnitude better. Previous studies on Ni^{2+} systems have also encountered this problem,[31] and it has been explained by a differential nephelauxetic effect.[32] Thus, our simple model
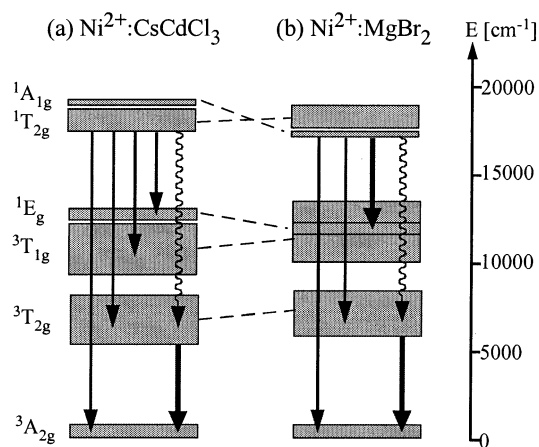

Figure 11. d–d energy level diagrams for Ni^{2+}:CsCdCl$_3$ (a) and Ni^{2+}:MgBr$_2$ (b). The solid downward arrows represent luminescence transitions. The dominant spin-allowed ones are indicated by the strong arrows. The wavy arrows represent multiphonon relaxation processes.

cannot accurately describe the energetic difference between the $^1A_{1g}$ and $^1T_{2g}$ excited states.

B. Crystal Field Effects on the Higher Excited-State Luminescence Properties. The 15 K survey luminescence spectrum of 0.1% Ni^{2+}:CsCdCl$_3$ in Figure 3a is representative of low-temperature Ni^{2+} luminescence in chlorides[6,33] and fluorides,[5] as well as oxides.[4] Luminescence transitions from the $^1T_{2g}$ state occur to all energetically lower lying electronic states, as schematically illustrated by the faint straight arrows in Figure 11a. The two highest energy luminescence bands in Figure 3a are due to $^1T_{2g} \rightarrow {}^3A_{2g}$ and $^1T_{2g} \rightarrow {}^3T_{2g}$ emission and correspond to the well-known green and red emissions in Ni^{2+}-doped fluorides and oxides.[4] In Ni^{2+}:CsCdBr$_3$, Figure 3b, the two highest energy luminescence bands have band shapes very similar to those in Ni^{2+}:CsCdCl$_3$, Figure 3a, and they are attributed to the same luminescence transitions.[7,34] Both are red-shifted with respect to the chloride due to the strong reduction of the Racah parameters; see Table 3. The two highest energetic luminescence bands of 0.1% Ni^{2+}:MgBr$_2$, Figure 3d, exhibit fundamentally different shapes. Vis emission occurs in a very narrow spectral range, and this is typical for so-called spin-flip transitions. Thus, its band shape as well as its energetic position relative to $^3A_{2g} \rightarrow {}^1A_{1g}$ absorption, Figures 2d/4, are consistent with an assignment to $^1A_{1g} \rightarrow {}^3A_{2g}$ luminescence. The broad-band luminescence centered at 10 400 cm^{-1} is assigned to $^1A_{1g} \rightarrow {}^3T_{2g}$ emission. This is a transition between states with different slopes in Figure 1; i.e., it involves an electron promotion from a t$_{2g}$ to an e$_g$ orbital. This explains the width of the respective luminescence band. These two emission transitions are indicated by the faint straight arrows in Figure 11b. The most intense higher excited-state luminescence band of Ni^{2+}: MgBr$_2$, Figure 3d, is observed around 6300 cm^{-1}. From its energetic position, its narrow band shape, and its relative intensity compared to the higher energetic luminescence

(25) Ferguson, J.; Guggenheim, H. J.; Tanabe, Y. *J. Chem. Phys.* **1965**, *47*, 775–786.
(26) (a) Bussière, G.; Reber, C. *J. Am. Chem. Soc.* **1988**, *110*, 6306–6315. (b) Bussière, G.; Beaulac, R.; Cardinal-David, B.; Reber, C. *Coord. Chem. Rev.* **2001**, *219–221*, 509–543.
(27) Liehr, A. D.; Ballhausen, C. J. *Ann. Phys.* **1959**, *2*, 134–155.
(28) Shannon, R. D. *Acta Crystallogr., Sect. A* **1976**, *32*, 751–767.
(29) (a) Jørgensen, C. K. *Prog. Inorg. Chem.* **1962**, *4*, 73–124. (b) König, E. *Struct. Bonding* **1970**, *7*, 175–212.
(30) Knox, K.; Shulman, R. G.; Sugano, S. *Phys. Rev.* **1963**, *130*, 512–516.
(31) Stranger, R.; McMahon, K. L.; Gahan, L. R.; Bruce, J. I.; Hambley, T. W. *Inorg. Chem.* **1997**, *36*, 3466–3475.

(32) Lohr, L. L. *J. Chem. Phys.* **1966**, *45*, 3611–3622.
(33) May, P. S.; Güdel, H. U. *Chem. Phys. Lett.* **1989**, *164*, 612–616.
(34) The unusual band shapes of the Ni^{2+} $^1T_{2g} \rightarrow {}^3T_{2g}$ and $^1T_{2g} \rightarrow {}^3T_{1g}$ inter-excited-state luminescence transitions have been discussed in detail in: May, P. S.; Güdel, H. U. *J. Chem. Phys.* **1991**, *95*, 6343–6354; *Chem. Phys. Lett.* **1990**, *175*, 488–492.

Table 4. Energies E_0 and Energy Differences ΔE_0 (in cm^{-1}) of the Electronic Origins of Various Metastable Excited States of Ni^{2+}

no.	transition	labels used in text	Ni^{2+}:CsCdCl$_3$	Ni^{2+}:CsCdBr$_3$	Ni^{2+}:CsMgBr$_3$	Ni^{2+}:MgBr$_2$
1[a]	$^3A_{2g} \rightarrow {}^3T_{2g}$	$E_0(^3T_{2g})$	4 970 ± 2	5302 ± 20	5 555 ± 20	5 630 ± 20
2[b]	$^3A_{2g} \rightarrow {}^1A_{1g}$	$E_0(^1A_{1g})$			16 919 ± 5	17 175 ± 5
3[c]	$^3A_{2g} \rightarrow {}^1T_{2g}$	$E_0(^1T_{2g})$	17 326			
4[d]	$^3T_{2g} \rightarrow {}^1A_{1g}$	$\Delta E_0(^1A_{1g}-^3T_{2g})$			11 355 ± 2	11 553 ± 2
5[d]	$^3T_{2g} \rightarrow {}^1T_{2g}$	$\Delta E_0(^1T_{2g}-^3T_{2g})$	12 344 ± 2[f]	11 240 ± 2	11 418 ± 2	11 694 ± 2
6[e]		$\Delta E_0(^1T_{2g}-^1A_{1g})$	<0	<0	63 ± 4	141 ± 4

[a] From 15 K ground-state absorption and luminescence data (Figures 2 and 3). [b] From Figure 4. [c] From published luminescence data.[10] [d] From the 15 K $^3T_{2g} \rightarrow {}^1A_{1g}/^1T_{2g}$ ESE spectra in Figures 9 and 10. [e] Calculated from $\Delta E_0(^1T_{2g}-^3T_{2g})$ (fifth row) minus $\Delta E_0(^1A_{1g}-^3T_{2g})$ (fourth row). [f] From published ESE spectra.[40]

bands it is assigned to spin-allowed $^1A_{1g} \rightarrow {}^1E_g$ emission; see the upper strong arrow in Figure 11b.

Vis luminescence of 0.1% Ni^{2+}:CsMgBr$_3$ contains both a sharp-line and a broad-band component. In the 15 K spectrum of Figure 3c their intensity ratio is roughly 10:1, respectively (see also Figure 6). We conclude that in this sample there is some $^1T_{2g}$ population already at 15 K. This is supported by the observation of $^1T_{2g} \rightarrow {}^3T_{1g}$ luminescence around 7200 cm^{-1} (compare to Figure 3b). Between 9500 and 11 500 cm^{-1} a luminescence band resembling $^1T_{2g} \rightarrow {}^3T_{2g}$ emission from Figure 3b is observed. We expect also $^1A_{1g} \rightarrow {}^3T_{2g}$ luminescence in this spectral region; see Figure 3d. Evidently the former is dominant, and we attribute this to a higher decay rate constant for $^1T_{2g} \rightarrow {}^3T_{2g}$ than for $^1A_{1g} \rightarrow {}^3T_{2g}$.

From a brief reinspection of the absorption spectra in Figure 2 we can rationalize the different higher excited-state luminescence properties observed for the three bromides. Although the decrease in the Racah parameters upon change from CsCdCl$_3$ to CsCdBr$_3$ as a host for Ni^{2+} leads to a reversed order of the $^1T_{2g}$ and $^1A_{1g}$ absorption band maxima, the electronic $^1T_{2g}$ origin is clearly at lower energy than the electronic $^1A_{1g}$ origin in Ni^{2+}:CsCdBr$_3$. The additional increase of 10Dq in Ni^{2+}:CsMgBr$_3$ and Ni^{2+}:MgBr$_2$ (Table 3) is needed to induce a crossover of the electronic origins.

C. Vibrational Fine Structure and Temperature Dependence of Vis Higher Excited-State Luminescence in Ni^{2+}:MgBr$_2$ and Ni^{2+}:CsMgBr$_3$. The site symmetry of Ni^{2+} in both MgBr$_2$ and CsMgBr$_3$ is D_{3d}; i.e., there is a center of inversion and electric-dipole (ED) d−d transitions are parity-forbidden. They gain their intensity by coupling to ungerade vibrations.[35] Thus, the most intense lines in the 15 K Ni^{2+} $^3A_{2g} \leftrightarrow {}^1A_{1g}$ absorption and luminescence spectra of Ni^{2+}:MgBr$_2$ in Figure 4 must be due to vibronic origins. The most prominent ones, labeled 5a/5e, are at 17 338 and 17 012 cm^{-1} in absorption and luminescence, respectively; see Table 2. It is plausible to assume that they are due to coupling to the same ungerade enabling mode. In this case, assuming the same vibrational energies in both $^3A_{2g}$ ground state and $^1A_{1g}$ excited state, the electronic $^1A_{1g}$ origin is expected at 17 175 cm^{-1}. In fact, all luminescence lines in Figure 4 located a certain amount of energy below 17 175 cm^{-1} have a counterpart in absorption located by an approximately equal amount of energy above 17 175 cm^{-1}; see Table 2. We conclude that the electronic $^1A_{1g}$ origin is at 17 175 ± 5 cm^{-1} (arrow in Figure 4). On the basis of published IR spectroscopy data on CsNiBr$_3$, the vibronic origins nos. 3 and 5 are assigned to e$_{1u}$ and a$_{2u}$ modes of D_{6h}^4 factor group.[36] The

absorption and luminescence lines 6a/e are about 150 cm^{-1} above and below the prominent 5a/e lines, respectively. This corresponds to the ground state a$_{1g}$ vibrational energy of the MBr$_6^{4-}$ unit in MgBr$_2$,[37] and thus the lines 6a/e are assigned to a$_{1g}$ vibrational sidebands built on the strong vibronic origins 5a/e. From the intensity ratio of lines 5 and 6 a Huang−Rhys parameter $S = 0.06$ is obtained.[38] This translates to a Ni^{2+}−Br$^-$ distance increase of only 0.008 Å upon $^3A_{2g} \rightarrow {}^1A_{1g}$ photoexcitation,[39] and this highlights the essentially pure spin-flip character of this electronic transition.

An analogous analysis of the 15 K $^3A_{2g} \leftrightarrow {}^1A_{1g}$ transitions can be made for Ni^{2+}:CsMgBr$_3$ (high-resolution data not shown). The main result from this analysis is that the electronic $^1A_{1g}$ origin is located at 16 919 ± 5 cm^{-1} in Ni^{2+}:CsMgBr$_3$, i.e., 256 cm^{-1} lower than in Ni^{2+}:MgBr$_2$; see the second row in Table 4. Finally, we note that previous EPR studies have reported $^3A_{2g}$ ground-state zero field splittings of 1.28 and 1.70 cm^{-1} for Ni^{2+}:CsCdBr$_3$ and Ni^{2+}:CsMgBr$_3$,[41] but these splittings are too small to be resolved in our 15 K $^1A_{1g} \rightarrow {}^3A_{2g}$ luminescence spectra.

Above 15 K, the sharp-line vis luminescence intensity in 0.1% Ni^{2+}:MgBr$_2$ and 0.1% Ni^{2+}:CsMgBr$_3$ decreases rapidly, and there is a concomitant rise in broad-band vis luminescence between 15 000 and 17 000 cm^{-1}; see Figure 5. Figure 6 plots the ratio of broad-band (B) $^1T_{2g} \rightarrow {}^3A_{2g}$ versus sharp-line (S) $^1A_{1g} \rightarrow {}^3A_{2g}$ luminescence intensity on a logarithmic scale as a function of 1/T. At the lowest temperatures vis luminescence is dominated by sharp-line $^1A_{1g} \rightarrow {}^3A_{2g}$ emission. At elevated temperatures, there is a nonnegligible $^1T_{2g}$ population, and this leads to broad $^1T_{2g} \rightarrow {}^3A_{2g}$ emission. Thus, there is a competition between $^1A_{1g}$ and $^1T_{2g}$ emission. From the temperature dependence of the ratios B/S we can obtain information about the energetic separation of the electronic $^1A_{1g}$ and $^1T_{2g}$ origins and about the relative radiative decay rate constants of $^1A_{1g} \rightarrow {}^3A_{2g}$ and $^1T_{2g} \rightarrow {}^3A_{2g}$ emission in Ni^{2+}:MgBr$_2$ and Ni^{2+}:CsMgBr$_3$. We point out that the $^1T_{2g}$ state is split into ^1E_g and $^1A_{1g}$ components by the trigonal crystal field. By $^1T_{2g}$ origin we denote the

(35) Herzberg, G.; Teller, E. *Z. Phys. Chem. B* **1933**, *21*, 410−446.
(36) McPherson, G. L.; Chang, J. R. *Inorg. Chem.* **1973**, *12*, 1196−1198.
(37) Anderson, A.; Lo, Y. W. *Spectrosc. Lett.* **1981**, *14*, 603−615.
(38) Huang, K.; Rhys, A. *Proc. R. Soc. London A* **1950**, *204*, 406−423.
(39) Determined from ν(a$_{1g}$) = 151 cm^{-1}, μ = 79.9 amu, and the modal description Q (Å) = ≈6$^{1/2}r$ (Å). Wilson, R. B.; Solomon, E. I. *Inorg. Chem.* **1978**, *17*, 1729−1736.
(40) Wenger, O. S.; Güdel, H. U. *Inorg. Chem.* **2001**, *40*, 157−164.
(41) McPherson, G. L.; Devaney, K. O. *Inorg. Chem.* **1977**, *16*, 1565−1568.

Table 5. Energetic Separation ΔE of the Electronic $^1A_{1g}$ and $^1T_{2g}$ Origins and Ratios k_B/k_S of Radiative Decay Rate Constants for $^1T_{2g} \rightarrow$ $^3A_{2g}$ (B) versus $^1A_{1g} \rightarrow ^3A_{2g}$ (S) Emission Extracted from Fits with Eq 3 to the Data in Figure 6

	Ni²⁺:MgBr₂	Ni²⁺:CsMgBr₃
$\Delta E/cm^{-1}$	169	67
k_B/k_S	12.2	13.5

electronic origin of the lower energetic trigonal component. The fact that nonradiative relaxation processes become increasingly active at elevated temperatures, section IVD, does not affect this discussion as long as we are concerned with $^1A_{1g} \rightarrow ^3A_{2g}$ versus $^1T_{2g} \rightarrow ^3A_{2g}$ photon ratios. We use the simplified model in the inset of Figure 6 to analyze our data.[42] The energetic difference between the electronic $^1A_{1g}$ and $^1T_{2g}$ origins is designated ΔE. The intrinsic radiative decay rate constants for $^1A_{1g} \rightarrow ^3A_{2g}$ and $^1T_{2g} \rightarrow ^3A_{2g}$ luminescence (left and right downward arrows) are designated k_S and k_B, respectively. The photon ratio B/S is given by

$$\frac{B}{S} = \frac{k_B N_B}{k_S N_S} \tag{1}$$

where N_B/N_S is the ratio of the $^1T_{2g}$ and $^1A_{1g}$ Boltzmann populations. It is calculated as[43]

$$\frac{N_B}{N_S} = 3 \exp\left(-\frac{\Delta E}{kT}\right) \tag{2}$$

where the factor of 3 stems from the 3-fold degeneracy of $^1T_{2g}$. Combining eqs 1 and 2, one obtains

$$\ln\left(\frac{B}{S}\right) = A - \frac{\Delta E}{kT} \tag{3}$$

where $A = \ln(3k_B/k_S)$. Thus, linear regression fits to the experimental $\ln(B/S)$ versus $1/T$ data in Figure 6 yield values for A and $\Delta E/k$. We obtain $\Delta E = 169$ cm⁻¹ for Ni²⁺:MgBr₂ (circles) and $\Delta E = 67$ cm⁻¹ for Ni²⁺:CsMgBr₃ (squares); see Table 5. The higher ΔE value for Ni²⁺:MgBr₂ reflects the stronger crystal field in this system; see Table 3. A is 3.6 and 3.7 for Ni²⁺:MgBr₂ and Ni²⁺:CsMgBr₃, respectively, and this yields k_B/k_S ratios of 12.2 and 13.5; see Table 5. Since there is a direct relation between radiative decay rate constants and oscillator strengths,[43] our k_B/k_S ratios can also be calculated from the experimental ratio of the $^3A_{2g} \rightarrow ^1T_{2g}$ (f_B) versus $^3A_{2g} \rightarrow ^1A_{1g}$ (f_S) oscillator strengths in Table 1 using

$$\frac{k_B}{k_S} = \frac{f_B}{f_S} \frac{g_S}{g_B} \left(\frac{\lambda_S}{\lambda_B}\right)^2 \tag{4}$$

where g_S and g_B are the degeneracies of the $^1A_{1g}$ (1) and $^1T_{2g}$ (3) states, respectively, and the trigonal splitting of $^1T_{2g}$

(42) (a) Jacobsen, S. M.; Güdel, H. U.; Daul, C. A. *J. Am. Chem. Soc.* **1988**, *110*, 7610−7616. (b) Wenger, O. S.; Güdel, H. U. *Chem. Phys. Lett.* **2002**, *354*, 75−81. (c) Wamsley, P. R.; Bray, K. L. *J. Lumin.* **1994**, *59*, 11−17.
(43) See for example: Brunold, T. C.; Güdel, H. U. *Inorganic Electronic Structure and Spectroscopy*; Solomon, E. I., Lever, A. B. P., Eds.; Wiley: New York, 1999; pp 259−306.

is neglected. λ_S and λ_B are the average emission wavelengths of $^1A_{1g} \rightarrow ^3A_{2g}$ (585 nm) and $^1T_{2g} \rightarrow ^3A_{2g}$ (641 nm) luminescence, respectively. Thus, one obtains $k_B/k_S = 9.0$ for Ni²⁺:MgBr₂ and 10.4 for Ni²⁺:CsMgBr₃. Both values are in reasonable agreement with those in Table 5 (12.2 and 13.5, respectively) extracted from the vis luminescence temperature dependencies.

D. Thermally Induced Nonradiative Relaxation from the Metastable $^1A_{1g}/^1T_{2g}$ and $^3T_{2g}$ Excited States. Nonradiative relaxation processes in Ni²⁺-doped CsCdCl₃ and a series of other Ni²⁺-doped chlorides have been studied in detail previously.[6] Therefore, we focus on the bromide systems in this section. The drops of the $^1A_{1g}/^1T_{2g} \rightarrow ^3A_{2g}$ luminescence intensities with increasing temperature, Figure 7b, are accompanied by a corresponding decrease of the luminescence lifetimes (data not shown). This is clear evidence for the onset of nonradiative relaxation processes with increasing temperature. The same is true for the $^3T_{2g}$ depopulation at elevated temperatures; see Figure 7a. All data in Figure 7 are obtained from only 0.1% Ni²⁺-doped crystals. Cross-relaxations are thus not efficient $^1A_{1g}/^1T_{2g}$ depopulation processes,[6] and we attribute the thermally induced luminescence quenching in our systems to multiphonon relaxation, i.e., a transformation of the electronic excitation energy into vibrational energy and thus ultimately into heat.[44] These processes have their physical origin in the electron/phonon coupling.

The filled circles in Figure 8 mark the quenching temperature $T_Q(^3T_{2g})$ for NIR $^3T_{2g} \rightarrow ^3A_{2g}$ luminescence in Ni²⁺:CsCdBr₃, Ni²⁺:CsMgBr₃, and Ni²⁺:MgBr₂ as a function of $10Dq$ in these systems (see Table 3). We observe a linear correlation of $T_Q(^3T_{2g})$ and $10Dq$. This is in line with a previous study on a series of Ni²⁺-doped chloride systems, where $T_Q(^3T_{2g})$ increases linearly with increasing $10Dq$, too.[21]

Whereas $^3T_{2g}$ depopulation in Ni²⁺-doped halide systems typically occurs purely radiatively below 100 K,[21,45] $^1T_{2g}/^1A_{1g}$ higher excited state depopulation typically contains both radiative and nonradiative components even at 15 K. For the three bromide systems considered here, this becomes obvious when comparing the $^3T_{2g} \rightarrow ^3A_{2g}$ luminescence intensities and the $^1A_{1g}/^1T_{2g} \rightarrow ^3T_{2g}$, $^3T_{1g}(^3F)$, and ^1E_g higher excited-state luminescence intensities in the survey luminescence spectra of Figure 3b−d. In all three bromides excitation into $^3T_{1g}(^3P)$ induces substantially more $^3T_{2g} \rightarrow ^3A_{2g}$ luminescence than $^1A_{1g}/^1T_{2g} \rightarrow ^3T_{2g}$, $^3T_{1g}(^3F)$, and ^1E_g luminescence. In 0.1% Ni²⁺:MgBr₂ and 0.1% Ni²⁺:CsMgBr₃ at 15 K this photon ratio is about 5:1, and in 0.1% Ni²⁺:CsCdBr₃ it is roughly 40:1. From this we conclude that efficient $^1A_{1g}/^1T_{2g} \rightarrow ^3T_{2g}$ multiphonon relaxation processes (wavy downward arrows in Figure 11) occur in all these systems already at 15 K. This is in line with previous studies on Ni²⁺:CsCdCl₃ and other Ni²⁺-doped chlorides.[6] The above photon ratios indicate that at 15 K these multiphonon relaxation processes are more efficient in 0.1% Ni²⁺:CsCdBr₃ than in 0.1% Ni²⁺:CsMgBr₃ and 0.1% Ni²⁺:MgBr₂. This is

(44) *Radiationless Processes*; Nato Advanced Study Institutes Series B62; Di Bartolo, B., Ed.; Plenum: New York, 1979.
(45) Reber, C.; Güdel, H. U. *Inorg. Chem.* **1986**, *25*, 1196−1201.

Table 6. 15 K Lifetimes of the Metastable Excited States of Ni^{2+} in the Bromide Hosts with Dopant Concentrations of 0.1%

	Ni^{2+}:$CsCdBr_3$	Ni^{2+}:$CsMgBr_3$	Ni^{2+}:$MgBr_2$
$^3T_{2g}$/ms	3.2	2.9[a]	3.9
$^1A_{1g}$/$^1T_{2g}$/μs	3.2	64.3	53.8

[a] From ref 45.

supported by the 15 K $^1A_{1g}$/$^1T_{2g}$ lifetime data in Table 6. The 15 K $^1T_{2g}$ lifetime of 0.1% Ni^{2+}:$CsCdBr_3$ is about a factor of 20 shorter than the 15 K $^1A_{1g}$ lifetimes of 0.1% Ni^{2+}:$CsMgBr_3$ and 0.1% Ni^{2+}:$MgBr_2$. Thus, we estimate that at 15 K multiphonon relaxation from $^1T_{2g}$ in 0.1% Ni^{2+}:$CsCdBr_3$ is roughly 20 times more efficient than from $^1A_{1g}$ in 0.1% Ni^{2+}:$CsMgBr_3$ and 0.1% Ni^{2+}:$MgBr_2$. Consequently, in Figure 7b the temperature-dependent $^1T_{2g}$ emission intensity data of 0.1%Ni^{2+}:$CsCdBr_3$ (triangles) are normalized to a maximum value of 1/20 at 15 K. The $^1T_{2g}$ luminescence quenching temperature $T_Q(^1T_{2g})$ as defined in section III is thus below 15 K for this system. In Figure 8 we assume a value of 5 K.

The plot of $T_Q(^1T_{2g}/^1A_{1g})$ versus $10Dq$ in Figure 8 (filled squares) and the included linear regression fit (lower line) indicate that there is a linear correlation between these two quantities, very similar to the correlation between $T_Q(^3T_{2g})$ and $10Dq$; see above. We explain these correlations with an increasing energetic separation of the emitting states and their energetically next lower lying states with increasing $10Dq$.

E. Excited-State Absorption Transitions Originating from $^3T_{2g}$. ESA transitions from $^3T_{2g}$ in Ni^{2+}:$CsCdCl_3$ have been studied in detail previously.[9,40,46] Therefore we focus on the bromide systems in this section. From simple energetic considerations of the absorption spectra in Figure 2, in the $11\,000-14\,400$ cm^{-1} spectral range, one expects 3 excited-state absorption (ESA) transitions originating from $^3T_{2g}$, namely transitions to $^1A_{1g}$, $^1T_{2g}$, and $^3T_{1g}(^3P)$, respectively. In Figure 9 we observe complicated and relatively weak excited-state excitation (ESE) features around $11\,200-12\,000$ cm^{-1} and comparatively intense ESA bands above $13\,600$ cm^{-1}. These experimental ESE bands correspond to ESA transitions. According to their energies and relative intensities they are assigned to spin-forbidden $^3T_{2g} \rightarrow {}^1A_{1g}/^1T_{2g}$ and spin-allowed $^3T_{2g} \rightarrow {}^3T_{1g}(^3P)$ ESA, respectively. Their energies increase along the series Ni^{2+}:$CsCdBr_3$, Ni^{2+}:$CsMgBr_3$, and Ni^{2+}:$MgBr_2$, and this is due to the increasing crystal field strength along this series (see section IVA). Of particular interest in these ESE spectra are the lower energy bands, which contain information about the $^1A_{1g}$/$^1T_{2g}$ splittings. The 15 K $^3T_{2g} \rightarrow {}^1A_{1g}/^1T_{2g}$ ESE bands of 0.1% Ni^{2+}:$CsMgBr_3$ are shown in more detail in Figure 10. In this system as well as in all other systems considered in this study, the $^3T_{2g}$ state is split by the trigonal crystal field into a $^3A_{1g}$ and a ^3E_g component. On the basis of 15 K polarized $^3A_{2g} \rightarrow {}^3T_{2g}$ absorption measurements on Ni^{2+}:$CsMgBr_3$, it has previously been concluded that the $^3A_{1g}$ component is energetically lower than the ^3E_g component by several hundred wavenum-

bers.[45] Consequently, at 15 K ESA transitions in Ni^{2+}:$CsMgBr_3$ originate exclusively from the origin of the $^3A_{1g}$ component, for simplicity hereafter referred to as the $^3T_{2g}$ origin. It is located at $E_0(^3T_{2g}) = 5555 \pm 20$ cm^{-1}; see the first row in Table 4. The lowest energetic weak line in Figure 10 at $11\,355 \pm 2$ cm^{-1} (see arrow no. 1) is assigned to the electronic origin of $^3T_{2g} \rightarrow {}^1A_{1g}$ ESA ($\Delta E_0(^1A_{1g}-^3T_{2g})$); see the fourth row in Table 4. Thus, $E_0(^3T_{2g}) + \Delta E_0(^1A_{1g}-^3T_{2g})$ $= 16\,910 \pm 22$ cm^{-1}, and this is in good agreement with the $E_0(^1A_{1g})$ value of $16\,919 \pm 5$ cm^{-1} (second row in Table 4) extracted from 15 K absorption and luminescence spectra; see section IVC. The intense line at $11\,418 \pm 2$ cm^{-1} in Figure 10 (see arrow no. 2) is assigned to the electronic origin of $^3T_{2g} \rightarrow {}^1T_{2g}$ ESA ($\Delta E_0(^1T_{2g}-^3T_{2g})$); see the fifth row in Table 4.[47] This assignment is supported by the fact that it yields an energetic splitting of the electronic $^1T_{2g}$ and $^1A_{1g}$ origins $\Delta E_0(^1T_{2g}-^1A_{1g})$ of 63 ± 4 cm^{-1}; see the sixth row in Table 4. This is in excellent agreement with the value of 67 cm^{-1} extracted from the VIS luminescence temperature dependence in Figure 6/Table 5.

An analogous analysis of the origin region of the 15 K $^3T_{2g} \rightarrow {}^1A_{1g}/^1T_{2g}$ ESE spectrum of 0.1% Ni^{2+}:$MgBr_2$ (not shown in detail; survey spectrum in Figure 9c) yields the following results. The lowest energetic weak absorption line is at $11\,553 \pm 2$ cm^{-1} (fourth row of Table 4), and it is assigned to the electronic $^3T_{2g} \rightarrow {}^1A_{1g}$ origin. The next lower lying line is at $11\,694 \pm 2$ cm^{-1} and more than 1 order of magnitude more intense than the $11\,553$ cm^{-1} line. It is assigned to the electronic $^3T_{2g} \rightarrow {}^1T_{2g}$ origin; see the fifth column in Table 4. From this we conclude that in Ni^{2+}:$MgBr_2$ the electronic $^1T_{2g}$ origin is 141 ± 4 cm^{-1} above the $^1A_{1g}$ origin; see the sixth column in Table 4. This compares to a value of 169 cm^{-1} extracted from the temperature-dependent luminescence data in Figure 6; see Table 5.

We turn our attention back to Figure 10 for a discussion of the observed vibrational sideband structure in the $^3T_{2g} \rightarrow {}^1A_{1g}/^1T_{2g}$ ESE bands of Ni^{2+}:$CsMgBr_3$. The $^3T_{2g} \rightarrow {}^1A_{1g}$ transition involves an electron promotion from an e_g to a t_{2g} orbital; see Figure 1. Thus, a relatively large Huang−Rhys parameter is expected for this transition.[48] Consequently, we assign the broad band centered around $11\,740$ cm^{-1} to $^3T_{2g} \rightarrow {}^1A_{1g}$ ESA. In the $11\,300-11\,640$ cm^{-1} range we have extrapolated its band shape; see the faint line in Figure 10. The intense sharp lines between $11\,418$ and $11\,600$ cm^{-1} are then all due to $^3T_{2g} \rightarrow {}^1T_{2g}$ ESA. Evidently, the Huang−Rhys parameter for this transition is substantially smaller than for $^3T_{2g} \rightarrow {}^1A_{1g}$. It is essentially a spin-flip transition (see the parallel slopes of $^3T_{2g}$ and $^1T_{2g}$ in Figure 1), and we attribute the majority of sharp lines to vibronic origins. No regular vibrational progressions can be identified.

The 15 K $^3T_{2g} \rightarrow {}^1A_{1g}/^1T_{2g}$ ESE spectrum of Ni^{2+}:$CsCdBr_3$, Figure 9a, is very similar to that of Ni^{2+}:$CsMgBr_3$. Its lowest energetic line occurs at $11\,240 \pm 2$ cm^{-1}, and this corre-

(46) (a) Wenger, O. S.; Salley, G. M.; Valiente, R.; Güdel, H. U. *Phys. Rev. B* **2002**, *65*, 212108/1−4. (b) Wenger, O. S.; Valiente, R.; Güdel, H. U. *High-Pressure Res.* **2002**, *22*, 57−62.

(47) Note that also $^1T_{2g}$ is split into two trigonal components. With "$^1T_{2g}$ origin" we denote the electronic origin of the lower energetic trigonal $^1T_{2g}$ component.
(48) Ballhausen, C. J. *Introduction to Ligand Field Theory*; McGraw-Hill: New York, 1962.

sponds to the electronic $^3T_{2g} \rightarrow {}^1T_{2g}$ origin (fifth row in Table 4). In contrast to Ni²⁺:CsMgBr₃ and Ni²⁺:MgBr₂ a weak line corresponding to the $^1A_{1g}$ origin is not observed since it lies at higher energies than $^1T_{2g}$ in Ni²⁺:CsCdBr₃; see section IVB. In analogy to Ni²⁺:CsMgBr₃, the broad ESE band at 11 550 cm⁻¹ is assigned to $^3T_{2g} \rightarrow {}^1A_{1g}$ ESA, whereas the lower energy sharp features are attributed to $^3T_{2g} \rightarrow {}^1T_{2g}$.

In Ni²⁺:MgBr₂ the band shape of the 15 K $^3T_{2g} \rightarrow {}^1A_{1g}/{}^1T_{2g}$ ESE, Figure 9c, is very different from Ni²⁺:CsCdBr₃ and Ni²⁺CsMgBr₃, Figure 9a,b. In the latter two systems the 15 K $^3T_{2g} \rightarrow {}^1A_{1g}/{}^1T_{2g}$ ESE bands span a total range of roughly 800 cm⁻¹. In Ni²⁺:MgBr₂ they extend from 11 700 to 14 000 cm⁻¹, with two maxima: one around 11 700 cm⁻¹ and one around 13 000 cm⁻¹; see Figure 9c. A possible reason for this difference is the fact that the trigonal splitting of the $^3T_{2g}$ first excited state in Ni²⁺:MgBr₂ on one hand and Ni²⁺:CsMgBr₃ and Ni²⁺:CsCdBr₃ on the other hand is opposite. This statement is based on polarized 15 K $^3A_{2g} \rightarrow {}^3T_{2g}$ absorption experiments on oriented crystals (data not shown).[49] ESA transitions in Ni²⁺:MgBr₂ originate from the ^3E_g component of $^3T_{2g}$ whereas in Ni²⁺:CsMgBr₃ and Ni²⁺:CsCdBr₃ they originate from the $^3A_{1g}$ component (see above). This can lead to the observed different band shapes.

We turn to a short analysis of the 15 K $^3T_{2g} \rightarrow {}^3T_{1g}(^3P)$ ESE bands in Figure 9. The signal-to-noise ratio in the spectrum of 0.1% Ni²⁺:CsCdBr₃, Figure 9a, is relatively low, and therefore we focus on the spectra of 0.1% Ni²⁺:CsMgBr₃ and 0.1% Ni²⁺:MgBr₂, Figure 9b,c. In both of them it is possible to identify progressions in a 155 ± 3 cm⁻¹ mode as well as in a 111 ± 3 cm⁻¹ mode. In 0.1% Ni²⁺:CsMgBr₃, Figure 9b, the latter is clearly the dominant one, whereas in 0.1% Ni²⁺:MgBr₂, Figure 9c, the vibrational progressions in both modes are similarly pronounced. This explains the different band shapes of the spectra of Figure 9b,c. We have already identified the 155 cm⁻¹ mode as due to the a_{1g} vibration; see section IVC. On the basis of published Raman data for NiBr₂, the 111 cm⁻¹ progression is assigned to the e_g mode of the NiBr₆⁴⁻ octahedron.[50] The occurrence of a vibrational e_g progression in the $^3T_{2g} \rightarrow {}^3T_{1g}(^3P)$ ESE spectra is a direct manifestation of a Jahn–Teller effect. Thus, the situation here is similar to Cr³⁺ and V²⁺ $^4T_{2g} \rightarrow {}^4T_{1g}(^4F)$ ESA transitions, where the T_{2g} and T_{1g} states are displaced relative to each other along the e_g coordinate.[51]

Finally, we point out that in all of the systems studied here, in the spectral overlap region of $^3A_{2g} \rightarrow {}^3T_{1g}(^3F)/{}^1E_g$ GSA and $^3T_{2g} \rightarrow {}^1A_{1g}/{}^1T_{2g}$ ESA, i.e., roughly between 11 200 and 12 500 cm⁻¹, vis higher excited-state luminescence can be induced using a single strong NIR excitation source. In ref 52 we report on such a NIR to vis photon upconversion process in Ni²⁺:MgBr₂.

V. Concluding Remarks

The main change when going from CsCdCl₃ to bromide host lattices for Ni²⁺ dopant ions is a drastic increase in the degree of covalency of the Ni²⁺–X⁻ bond. This manifests itself in a 10% reduction of the Racah electron repulsion parameters. Thus, for Ni²⁺-doped bromides substantially higher $10Dq/B$ ratios than in chlorides or fluorides are achieved, and this puts bromide systems close to the $^1T_{2g}/{}^1A_{1g}$ crossing point of the d⁸ Tanabe–Sugano energy level diagram in Figure 1. The size of the M²⁺ ion of the host material largely determines the magnitude of the crystal field strength $10Dq$ which the Ni²⁺ dopant ions experience. This determines whether a given Ni²⁺-doped bromide system is a $^1T_{2g}$ or a $^1A_{1g}$ emitter. These two classes of bromide materials are represented by Ni²⁺:CsCdBr₃ on one hand and Ni²⁺:CsMgBr₃ and Ni²⁺:MgBr₂ on the other hand. The situation in Ni²⁺-doped bromides is thus somewhat similar to Cr³⁺-doped fluorides where, depending on $10Dq$, either broad-band $^4T_{2g}$ or sharp-line ^2E_g emission is observed,[53] except for the fact that in our systems this crossover is not accompanied by a change in the spin multiplicity of the emitting state. Numerous other systems in which an increase of $10Dq$ induces a crossover in the emitting first excited state are known, e.g. Ti²⁺-doped chlorides and V³⁺-doped bromides.[13,14] An electronic crossover in an emitting higher excited state of a transition metal ion, on the other hand, is extremely unusual. To our knowledge, this has previously only been observed for Co²⁺ in tetrahedral oxo coordination.[54]

(49) In the linear-chain systems CsCdBr₃ and CsMgBr₃ the Ni²⁺ d_{z^2} orbital interacts with the empty $3p_z$ orbitals of the neighboring Cd²⁺/Mg²⁺ ions, leading to a reversed orbital energy order than expected when considering only the elongated NiBr₆⁴⁻ octahedron. See ref 45 and Hauser, A.; Güdel, H. U. *J. Lumin.* **1982**, *27*, 249–256. In MgBr₂ this effect cannot occur due to the different crystal structure of this system.

(50) Anderson, A.; Lo, Y. W.; Todoeschuk, J. P. *Spectrosc. Lett.* **1981**, *14*, 105–116.

(51) (a) Payne, S. A.; Chase, L. L; Wilke, G. D. *Phys. Rev. B* **1988**, *37*, 998–1006. (b) Wenger, O. S.; Kück, S.; Güdel, H. U. *J. Chem. Phys.* **2002**, *117*, 909–913. (c) Lee, H. W. H.; Payne, S. A.; Chase, L. L. *Phys. Rev. B* **1989**, *39*, 8907–8914.

(52) Wenger, O. S.; Güdel, H. U. *Struct. Bonding*, in press.

(53) (a) Kenney, J. W., III; Clymire, J. W.; Agnew, S. F. *J. Am. Chem. Soc.* **1995**, *117*, 1645–1646. (b) Freire, P. T. C.; Pilla, O.; Lemos, V. *Phys. Rev. B* **1994**, *49*, 9232–9235.

(54) (a) Brunold, T. C.; Güdel, H. U.; Cavalli, E. *Chem. Phys. Lett.* **1996**, *252*, 112–120. (b) Donegan, J. F.; Anderson, F. G.; Bergin, F. J.; Glynn, T. J.; Imbusch, G. F. *Phys. Rev. B* **1992**, *45*, 563–573.